The International Journal of Advanced Manufacturing Technology (2020) 107:679–688
https://doi.org/10.1007/s00170-020-05062-x

ORIGINAL ARTICLE

Synthesis and characterization of non-equiatomic $Ti_{0.3}AlMoSi_{0.3}W_{0.1}$ high-entropy alloy fabricated via spark plasma sintering

L. R. Kanyane[1] · A. P. I. Popoola[1] · N. Malatji[1] · M. B. Shongwe[1]

Published online: 19 February 2020

Abstract
Failure of aerospace components from extreme operating temperatures due to oxidation in components such as turbine blades and compressor blades results in catastrophic consequences, which mostly lead to loss of lives and economic decline. Hence, a need for new novel materials with good corrosion, oxidation, and wear-resistant properties remains a necessity. Near-equiatomic $Ti_{0.3}AlMoSi_{0.3}W_{0.1}$ high-entropy alloy (HEA) with enhanced mechanical properties and good corrosion-resistant properties was synthesized by means of spark plasma sintering technology. The influence of spark plasma sintering temperature of developed $Ti_{0.3}AlMoSi_{0.3}W_{0.1}$ HEA was investigated at 800 °C, 900 °C, and 1000 °C. The microstructural evolution was studied by means of scanning electron microscope (SEM). The Vickers microhardness and wear-resistant properties were evaluated using diamond base microhardness tester (EMCO) and tribometer (Rtec), respectively. The corrosion resistance properties and oxidation resistance of the synthesized HEA were also evaluated in 0.5 M H_2SO_4 using 101 Autolab potentiostat/galvanostat devices and thermal gravimetric analyzer (TGA), respectively. Heat treatment effect on the synthesized HEA was also studied; the samples were exposed to high temperature of 900 °C in isothermal furnace with holding time of 8 h. From the results, it was found that fabricated HEA showed outstanding microhardness properties and good anticorrosion resistance properties in 0.5-M sulfuric acid medium.

Keywords High-entropy alloys (HEAs) · Anticorrosion · Wear · Oxidation microhardness

1 Introduction

Components in the jet engine must function consistently in difficult conditions and expand the boundaries of the material's capabilities [1]. The performance and safety are critical to the aircraft; therefore, the materials used in the main components of the aero engine such as the compressor blades serve an enormous role in the success of the aircraft [2]. Nevertheless, failure of the current commercial material (Ti6Al4V alloy) used in such application is restricted to non-friction occasions due to the low microhardness, poor wear resistance properties, and also poor oxidation properties at temperatures higher than 450 °C [3–10]. Hence, more demands for new materials with enhanced properties under harsh operating conditions are increasing.

HEAs remain promising multicomponent alloys which possess outstanding combination of mechanical and electrochemical properties applicable for advanced engineering application [11–14]. This is due to their nature of forming HEA single solid solution phase of BCC or FCC. However, Cantor [15] and Zhang [16] stated that not all the HEAs which consist of five or more elements with equiatomic or near equiatomic proportion fraction can practically result in HEA solid solutions. For the formation of BCC and FCC solid solution phases, carefully chosen compositions of the selected materials to be used in developing the alloy are important.

Mohanty et al. [17] reported the phase formation, microstructural evolution, and mechanical properties of a

✉ L. R. Kanyane
lrkanyane@gmail.com

A. P. I. Popoola
Malatjin@tut.ac.za

N. Malatji
popoolaapi@tut.ac.za

M. B. Shongwe
shongwemb@tut.ac.za

[1] Department of Chemical, Metallurgical and Materials Engineering, Tshwane University of Technology, P.M.B. X680, Pretoria, South Africa

multicomponent equiatomic AlCoCrFeNi high-entropy alloy synthesized by high-energy ball milling followed by spark plasma sintering. From the findings, the authors observed that the hardness of the sample increases with sintering temperature; the findings also showed that the AlCoCrFeNi HEA consisted of a face-centered cubic (FCC) phase and a duplex body-centered (BCC) structure. Kang et al. [18] studied ultra-high strength WNbMoTaV HEAs with fine grain structure fabricated by powder metallurgy. The findings proved that outstanding mechanical properties of the WNbMoTaV attributed primarily to intrinsic solid solution strengthening, with the combined effect of grain boundary strengthening and interstitial solid solution strengthening.

Numerous techniques are used to develop these classes of materials. However, spark plasma sintering (SPS) can readily produce a material of excellent mechanical properties by maintaining homogenous small grains where else arc melting results in a material that comprises of inhomogeneous coarse grains [19]. SPS is a sintering technique that uses uniaxial force and a pulsed direct electrical current under low atmospheric pressure to perform high-speed merging of the powder. It should be mentioned, however, that the final sintered material possesses increased brittleness due to densification [20]. It is, therefore, important to select a combination of metallic elements prior to sintering to produce a bulk material of several desirable properties [21].

The work aim to investigate the influence of sintering temperature on microhardness, densification, oxidation, wear, and corrosion properties of $Ti_{0.3}AlMoSi_{0.3}W_{0.1}$ HEA processed via spark plasma sintering. The effect of heat treatment procedure on microstructure and microhardness properties is also studied.

2 Experimental method

Ti, Al, Mo, Si, and W near equiatomic HEA powders were mixed using tubular mixer for a period of 8 h and poured into a graphite die of 40-mm diameter. The powder was then sintered using an SPS system (FCT Systeme GmbH, Rauenstein) at different sintering temperature. The HEA was sintered at a heating rate of 100 °C/min with a holding time of 8 min for each sintering temperature of 800, 900, and 1000 °C during sintering. Applied pressure of 50 MPa was used during the sintering process.

Sintered samples were then sandblasted, and the density of the 40-mm developed $Ti_{0.3}AlMoSi_{0.3}W_{0.1}$ HEAs was measured by Archimedes' method [7].

The synthesized HEA samples were cut transversely and mounted in an epoxy-based resin, polished using metallography procedures and etched with kroll agent solution for investigating the microstructural evolution of the developed alloys. The microstructures of $Ti_{0.3}AlMoSi_{0.3}W_{0.1}$ were characterized by means of scanning electron microscope. The phases present in the synthesized high-entropy alloys were identified using an X-ray diffractometer, and present phases were revealed using X-Pert High Score Plus software.

Emco TEST microhardness tester was used to measure the microhardness properties of the developed alloy. The indenting load of 100 kgf and a dwell time of 10 s were used. Tribological studies were examined using Rtech tribometer with a stainless steel contact ball. The applied force was 150 N for duration of 5 min.

The electrochemical behavior of the specimens was studied in 0.5 mol/L of H_2SO_4. The experiment was achieved using Autolab potentiostat equipped with Nova Software. Polarization curves were recorded at a start potential of 1.5 V to stop potential of − 1.5 V and at a scan rate of 0.001 mV/s.

Thermal gravimetric analyzer (TGA) was utilized to evaluate the effect of sintering temperature on the oxidation behavior of the fabricated high-entropy alloys. The fabricated alloy was studied at temperatures of between 45 and 900 °C. The heating rate of 10 °C/min was employed while feeding 20 mL/min of air. Thermal stability of the alloy was studied in an isothermal furnace with a holding time of 8 h.

3 Results and discussion

The experimental fabricated high-entropy alloy obtained for $Ti_{0.3}AlMoSi_{0.3}W_{0.1}$ is showed in Table 1. The applied pressure was kept at 50 MPa. Sintering temperature was varied, and holding time was 8 min.

3.1 Characterization of fabricated HEA

Figure 1 a–c presents the microstructure of the $Ti_{0.3}$-Al-Mo-$Si_{0.3}W_{0.1}$ HEA. All the HEA were sintered at 800, 900, and 1000 °C sintering temperature. The heating rate of the

Table 1 Summarized data of fabricated $Ti_{0.3}AlMoSi_{0.3}W_{0.1}$ HEA

Alloy	Temperature (°C)	Pressure (kPa)	Holding time (min)	Heating rate (°C/min)
$Ti_{0.3}$-Al-Mo-$Si_{0.3}W_{0.1}$	[3A] 800 [3B] 900 [3C] 1000	50	8	100

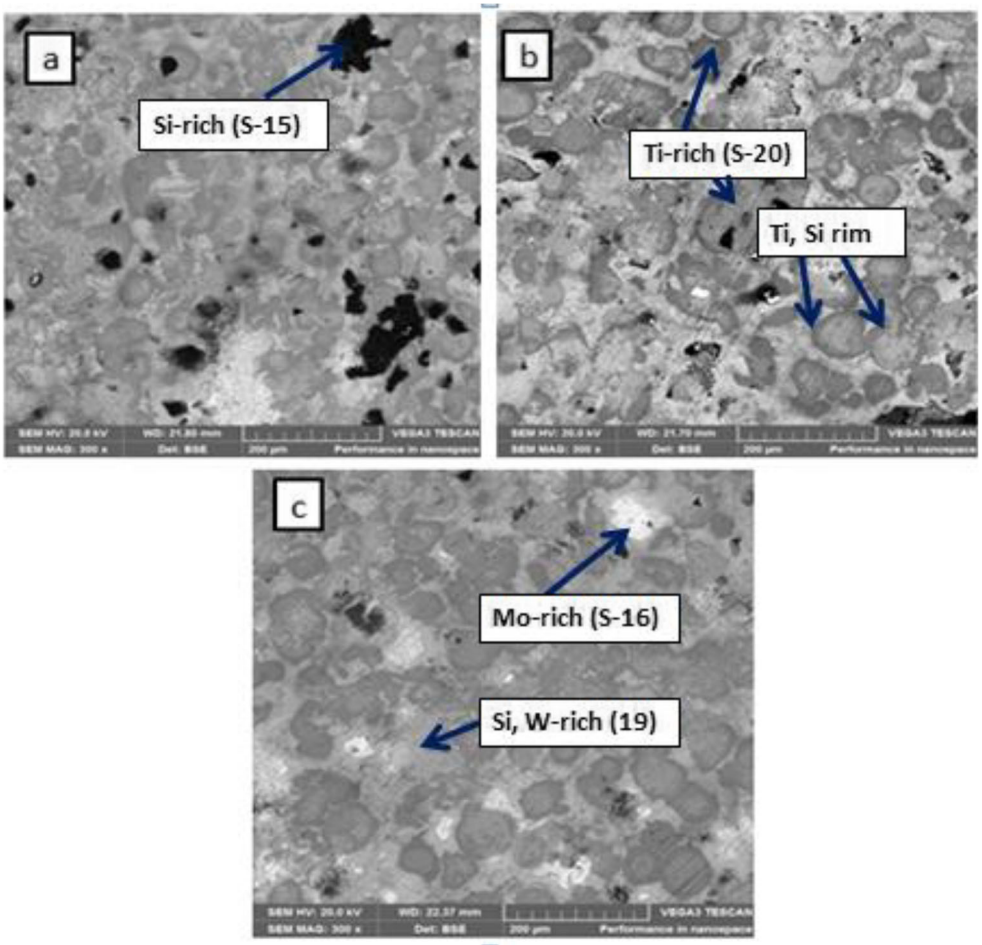

Fig. 1 SEM micrographs of $Ti_{0.3}$-Al-Mo-$Si_{0.3}W_{0.1}$ sintered high-entropy alloy at (**a**) 800 °C, (**b**) 900 °C, and (**c**) 1000 °C

sintering process was held at 100 °C/min at a holding time of 8 min under a pressure of 50 MPa. From the sintered micrograph, it is clear that the sintered materials contain three crystal structures with crystal boundaries; varying grain sizes and irregular shapes are clearly defined. The phases appear to be Ti, Si-rich gray phase, and W-rich whitish phase along with black Si-rich precipitates. Mo-rich phases begin to grow and distribute across the material at 900 °C. It is evident on the micrographs that an increase in sintering temperature results in dissolution of Si-rich phase which is in smaller quantity on the sample sintered at 1000 °C. Mo-rich phases begin to grow and distribute across the material at 900 °C. In all the presented SEM images, no cracks or initiation of stress can be identified.

Figure 2 presents the EDS of the $Ti_{0.3}$-Al-Mo-$Si_{0.3}W_{0.1}$ HEA. The EDS results confirm the presence of Ti, Al, Mo, Si, and W elemental powders which were used to consolidate HEA. Spectrum 15 proves to be Si-rich BCC phase. Spectrum 19 shows W and Si-rich BCC solid solution phase. The developed HEA are expected to show good strength due to the presence of the BCC structure present.

Yeh et al. [22] were the first to recommend that it is highly possible to produce simple solid solution phase of BCC or FCC structure when HEA which comprises of five or more elements owes to their high entropy of mixing. The high entropy of mixing can also inhibit the development of intermetallics alloys while facilitating the formation of solid solutions phases such as BCC and/or FCC. Table 2 presents the empirical calculation values of mixing enthalpy and entropy of $Ti_{0.3}$-Al-Mo-$Si_{0.3}W_{0.1}$ HEA. Zhang et al. (2008) proposed that most fabricated HEAs result in a formation of solid solution of BFF/FCC when $\Omega \geq 1.1$ and δ (%) $\leq 6.6\%$. It was showed from the empirical calculations that the values of the parameters of Ω and δ (%) are 0.569 and 2.634%, respectively. It is clear that Ω parameter breaks the solid solution formation rule, while δ (%) parameter well matches solid solution formation rules for the multi-principle HEAs proposed by Zhang et al. [16, 23].

Figure 3 presents XRD results of the synthesized HEA. Major peak consists of BCC solid solution phase along with ordered FCC phase of $TiSi_2$ and the intermetallics of Mo_2Si_3 and WSi_2. Combination of the FCC and BCC structure is expected to give good mechanical properties.

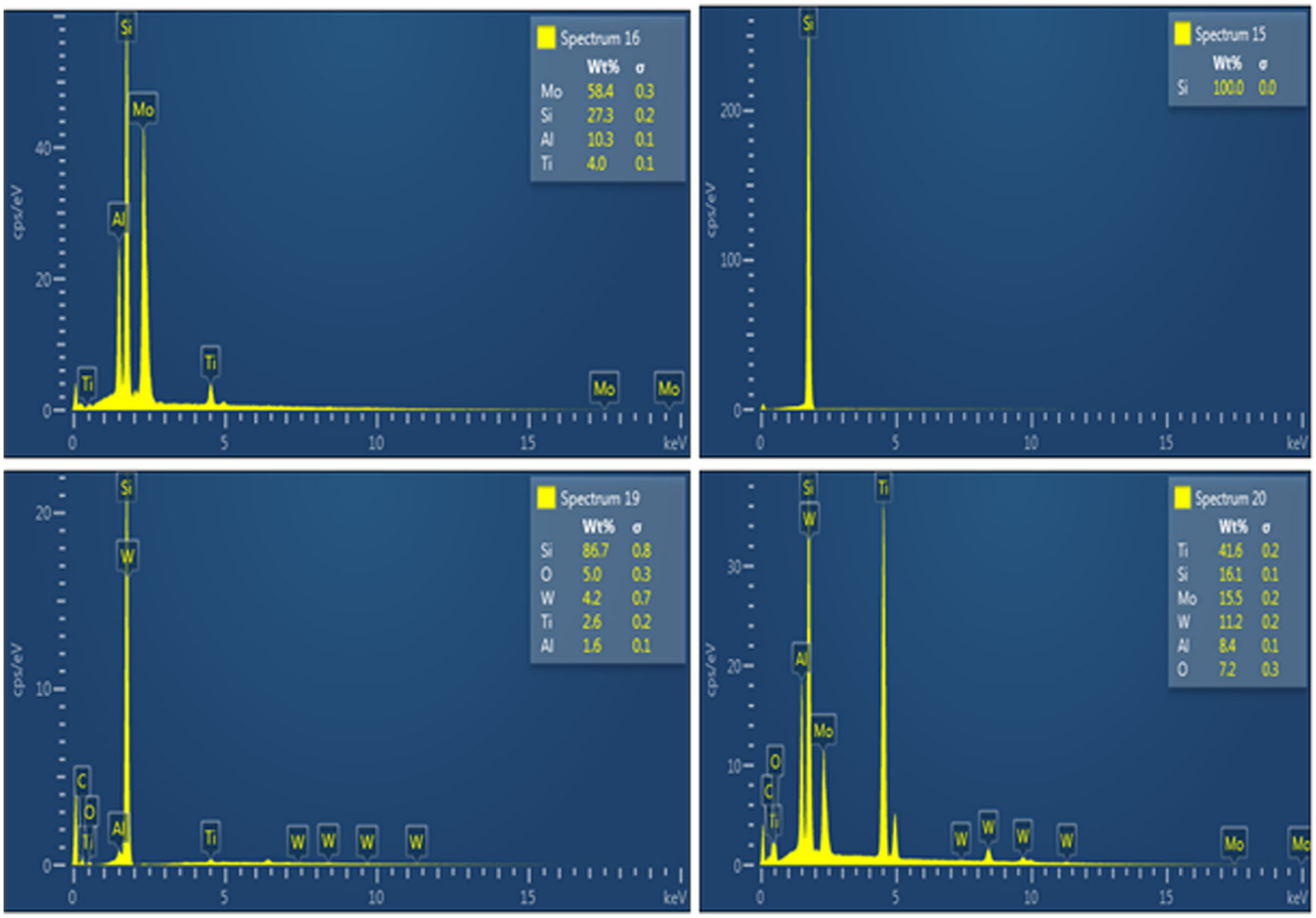

Fig. 2 EDS of $Ti_{0.3}$-Al-Mo-$Si_{0.3}W_{0.1}$ sintered high-entropy alloy at three different temperatures: (**a**) 800 °C, (**b**) 900 °C, and (**c**) 1000 °C

3.2 Microhardness and densification analysis

Figure 4 presents the microhardness properties and densification results of the synthesized $Ti_{0.3}$-Al-Mo-$Si_{0.3}W_{0.1}$ HEA. The developed HEA was sintered at sintering temperature of at 800, 900, 1000 °C, and the influence of sintering temperature on microhardness and densification is investigated.

High densification of above 96% is achieved for all sintered HEA samples at varying sintering temperatures. Furthermore, it can be observed from Fig. 4 that relative densification of fabricated HEA increases with increase in temperature. $Ti_{0.3}$-Al-Mo-$Si_{0.3}W_{0.1}$ HEA sintered at 1000 °C revealed a maximum densification of 98.86%, followed by samples sintered at 900 °C with 98.19% and at 800 °C with 96.42%, respectively. High densification results could be due to the fact that powders are subjected to high temperature which leads to high particle to particle diffusion and hence minimal porosity around the particles neck [7, 8, 24–26].

Table 2 The calculated values of parameters (ΔH_{mix}, ΔS_{mix}, T_m, δ, and Ω) for the investigated alloys

Alloy	ΔH_{mix} (KJ/mol)	ΔS_{mix} (JK^{-1} mol^{-1})	T_m (K)	δ (%)	Ω
$Ti_{0.3}$-Al-Mo-$Si_{0.3}W_{0.1}$	−45.18	12.652	2032.25	2.634	0.569

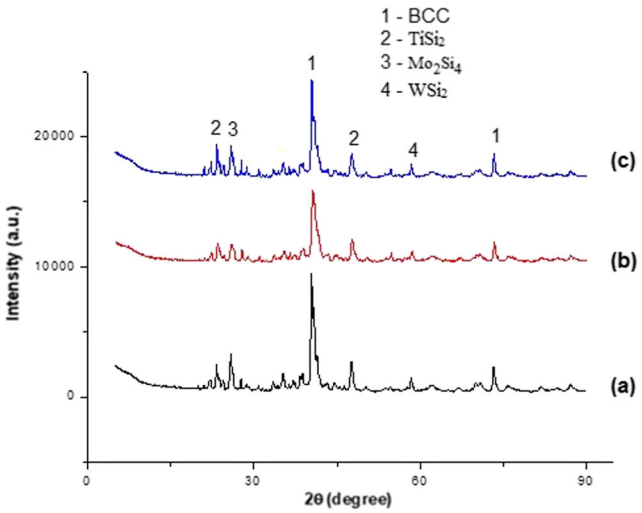

Fig. 3 XRD analysis of the developed $Ti_{0.3}$-Al-Mo-$Si_{0.3}W_{0.1}$ HEA

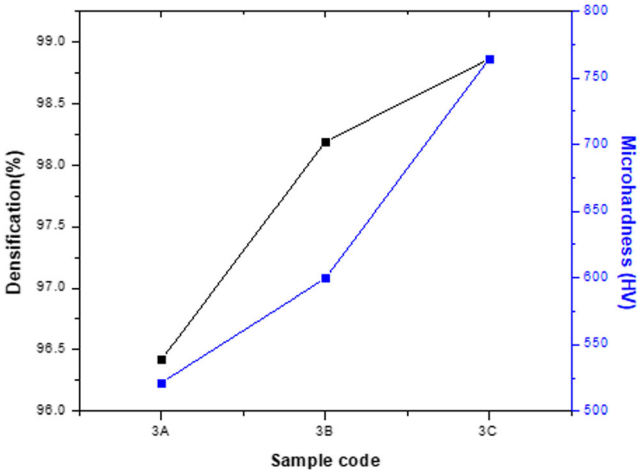

Fig. 4 Effect of sintering temperature on relative density and microhardness properties of synthesized HEA

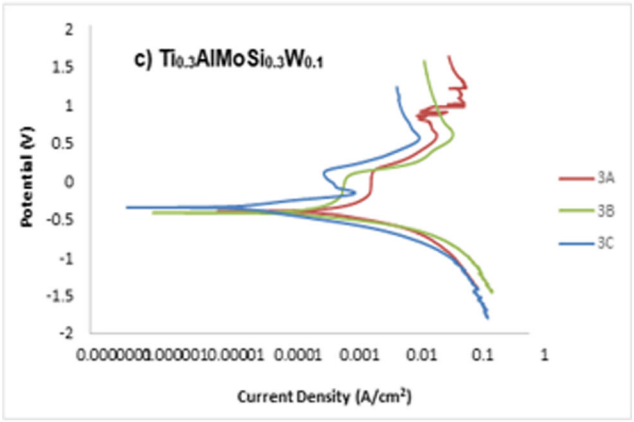

Fig. 6 Potentiodynamic polarization response of $Ti_{0.3}AlMoSi_{0.3}W_{0.1}$ HEA temperature in 0.5-M H_2SO_4 solution at room temperatures

The average microhardness values of the sintered HEA at varying temperatures were recorded as shown in Fig. 4. It can be noted that the highest obtained HV value was 764.63 HV and that the lowest being 521.44 HV at sintering temperatures of 1000 and 800 °C, respectively. The relationship between sintering temperature and microhardness is noticed. As sintering temperature increases, microhardness properties improve. High microhardness of the fabricated alloys can be attributed to factors such as sintering temperature and alloying elements presented in the HEA. Content of Al in developed HEAs encourages the formation of BCC phase and has stronger cohesive bonding with other elements [27]. W also plays an important role in microhardness properties of the multicomponent alloy as the element is known for been the hardest element on periodic table. Furthermore, the high microhardness properties can be justified by atomic radius of W (1.367 Å), Al (1.43 Å), Ti (1.47 Å), and Mo (1.363 Å) which are way larger than that of Si (1.15 Å). Larger atomic size difference in an alloy can result in increased lattice crystal distortion which can enhance the effect of solid solution strengthening [23, 28–30]. Additionally, it is known that the secondary phase precipitated from matrix phase can also interact with dislocations at the grains, which can easily hinder the dislocation movement remarkably, and hence high microhardness can be attained [31, 32]. BCC phase structure present in the HEA is known to possess good mechanical strength and ductility.

Figure 5 illustrates OPM indentions of the developed HEA sintered at various temperatures after microhardness test. From the micrographs, no cracking around the indentation surface is observed in all the synthesized HEA. Cracks around an indentation pyramid prove that the material is brittle. The slip mode at the indentation indicates that the samples have reasonable toughness. The developed HEA at both sintering temperatures presents good ductility since the alloy shows no cracks on the indent edges.

3.3 Electrochemical test results

Electrochemical studies were carried out on the $Ti_{0.3}$-Al-Mo-$Si_{0.3}W_{0.1}$ HEA. The samples were exposed in 0.5-M sulfuric acid. The corrosion resistance behaviors of the $Ti_{0.3}$-Al-Mo-$Si_{0.3}W_{0.1}$ HEAs sintered at different temperatures are

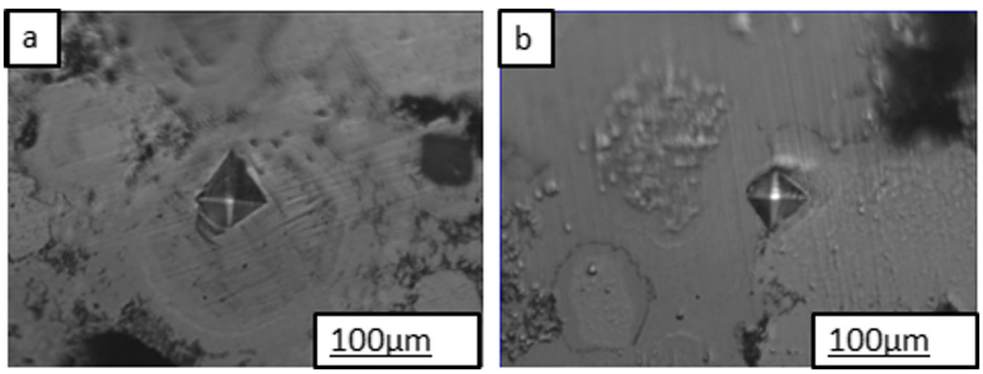

Fig. 5 OPM of the microhardness indentation. (**a**) 800 °C and (**b**) 1000 °C

Table 3 Alloy properties derived from potentiodynamic polarization curves by liner fit

HEA	Sintering temp (°C)	E_{corr} (V)	j_{corr} (A/cm^2)	Corrosion rate (mm/year)	Polarization resistance (Ω)
$Ti_{0.3}$-Al-Mo-$Si_{0.3}W_{0.1}$	3A – 800	− 0.48021	6.89E-03	0.00501	3710.01
	3B – 900	− 0.32564	2.58E-04	0.00581	3680.58
	3C – 1000	− 0.29784	3.9E-05	0.00426	3712.02

presented in Fig. 6, while Table 3 presents alloy properties derived from potentiodynamic polarization curves by liner.

Numerous investigated works pointed out that HEAs possess good corrosion behavior. This owes to the fact that HEAs have advantageous properties due to the alloying elements. The good corrosion resistance of the fabricated HEA might be ascribed to the fact that the alloying elements of Mo, Ti, and Al have a good corrosion resistance, and as a result, the protective film can be easily formed on the surface of the alloy and prevent it from further corroding. The anticorrosion properties of the synthesized alloys as all sintering temperature generally show good corrosion resistance in the corrosive medium. Highest polarization resistance (Rp) reached is 3712.02 Ω which is for the alloy fabricated at 1000 °C. This could be a result of a protective layer provided by titanium, molybdenum, and aluminum.

3.4 Thermal gravimetric test results

Figure 7 presents oxidation behavior of the fabricated $Ti_{0.25}$-Al-Mo-$Si_{0.25}W_{0.1}$ HEA examined in air from 40 to 900 °C and the sample weight change as a function of temperature. Heating rate of 10 °C/min was used while constantly feeding air at 20 mL/min. The initial sample weights are due to alterations which takes place during cutting of the samples.

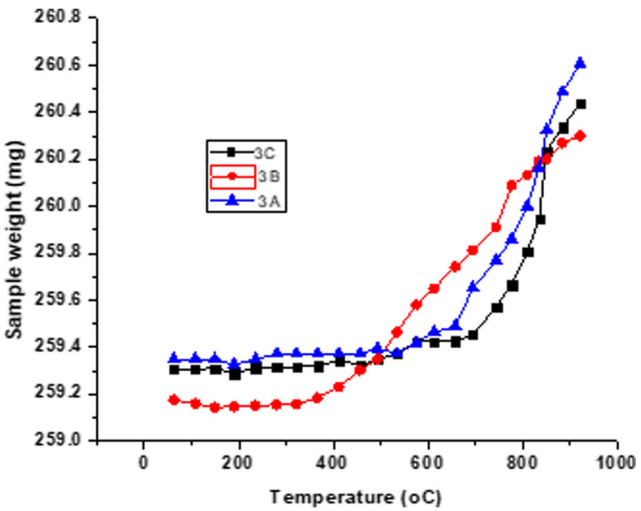

Fig. 7 Effect of sintering temperature on thermal stability of synthesized $Ti_{0.3}AlMoSi_{0.3}W_{0.1}$ HEA

Developed alloy sintered at 1000 °C shows a minimum mass gain of 1.21 mg as compared to samples sintered at 900 and 800 with mass gain of 1.29 mg and 1.36 mg, respectively. Sample 3A and 3C showed to be stable from 40 °C until 590 °C, and there was high degree of deflection at 590 °C which resulted from oxide scales forming on the alloy surface due to Ti, Al, and Si having high affinity for oxygen at high temperature. Good oxidation performance of the alloy can be attributed to that fact that high content of Ti and Al (30 at %) in HEAs helps with the formation of protective oxide films preventing the alloy to further oxidize [14].

Figure 8 also present SEM image of the oxidized surface of $Ti_{0.3}AlMoSi_{0.3}W_{0.1}$ developed HEA at (**a**) 800 °C and (**b**) 1000 °C. Morphological changes after exposing the samples to 900 °C while feeding air at 20 mL/min are minimal. The morphology of the alloys at both sintering temperatures shows stability. This is because the oxide of Ti, Al, and Mo elements is stable at higher temperature and they resist to further oxidase [14, 33, 34]. The initial XRD phase that showed $TiSi_2$ phase present in the HEA (Fig. 9) is known for its superior properties such as high melting point, low density, and good oxidation resistance [35]. The titanium silicide phase decomposed back to Ti and Si oxide phase after oxidation test. The entire element used to synthesize HEA system formed their oxide layer during exposure to air at high temperature. The developed scales of the SEM images could reasonably consist of TiO_2, SiO_2, Al_2O_3, MoO_3, and WO_3 oxide films which are evident on the XRD results.

3.5 Tribological performance

Figure 10 presents SEM wear scars of synthesized $Ti_{0.3}$-Al-Mo-$Si_{0.3}W_{0.1}$ HEA sintered at (**a**) 800 °C and (**b**) 1000 °C. Generally, all fabricated HEA showed better wear resistance properties due to high microhardness properties they possess. Both micrographs show moderate material loss with the sample sintered at 800 °C showing cracks at the grain boundaries of Ti-rich phase structure. Alloy sintered at low temperature is easy to go intense plastic deformation under normal and tangential force combined effect due to low hardness. It could be observed that at lower sintering temperature, the developed HEA shows severe peeling off of material as compared to samples sintered at 900 and 1000 °C. Alloy sintered at 1000 °C is highly resistant to plastic deformation which

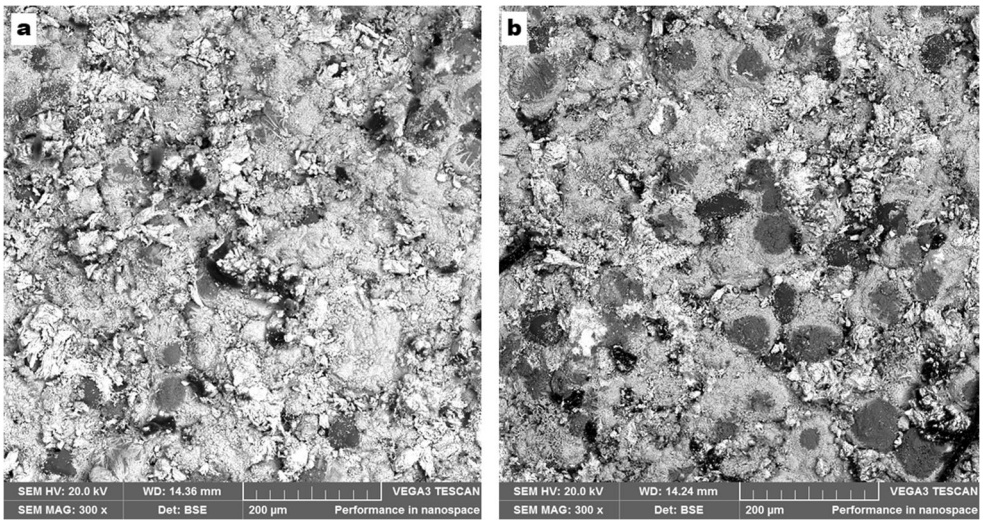

Fig. 8 SEM image of the oxidized surface of $Ti_{0.3}AlMoSi_{0.3}W_{0.1}$ developed HEA at (**a**) 800 °C and (**b**) 1000 °C

resulted in material loss on the alloy surface [36]. Figure 10 a also shows surface cracks present and on the other hand, Fig. 10 b shows material carryovers with minimal plastic deformation from the contact ball, and also adhered wear debris are present on the SEM image.

Figure 11 presents the variation of coefficient of friction (CoF) response of the synthesized alloys to the working load under sliding duration of the sample was 5 min with the applied load of 150 N. There is a clear relationship between CoF and the microhardness properties of the developed $Ti_{0.3}AlMoSi_{0.3}W_{0.1}$ HEA. High microhardness properties of the synthesized alloys resulted in low CoF hence less wear loss. The results also show the general trend between sintering temperature and the CoF. From all the synthesized alloys, as the sintering temperature increases, the CoF decreases. These may be attributed to the hardness test results. Minimum CoF was found to be 0.117 µ.

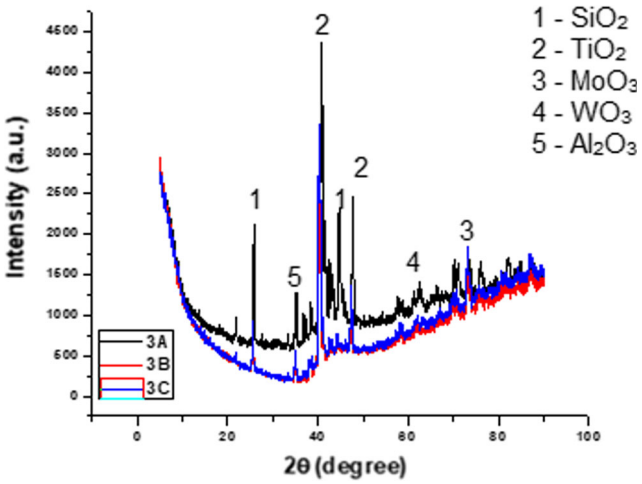

Fig. 9 XRD analysis of oxidized $Ti_{0.3}AlMoSi_{0.3}W_{0.1}$ HEA

3.5.1 Wear loss results

The wear loss of the fabricated $Ti_{0.3}AlMoSi_{0.3}W_{0.1}$ high-entropy alloy at varied sintering temperature was measured, and the graphs of the variation of the wear mass loss for all the $Ti_{0.3}AlMoSi_{0.3}W_{0.1}$ HEA sintered at 800, 900, and 1000 °C are presented in Fig. 12. From the near equiatomic ratio alloys, less wear mass loss of 0.00449 g was evident in the alloy sintered at 1000 °C, while alloy sintered at 800 °C showed a maximum wear loss of 0.00486 g. Effect of sintering temperature on the wear loss behavior of HEAs is recognized. At low sintering temperature, the rate of wear is high, while at high sintering temperature, the wear loss is lower. This may be attributed to the high degree of particle diffusion between high sintering temperature, which in turn results in different morphological evolution and hence different wear loss.

3.6 Microhardness of heat-treated HEA

The thermal stability of the synthesized HEA has been assessed using microhardness properties shown by Fig. 13. For this HEA, all heat-treatment methods resulted in increased microhardness. The synthesized HEA which were sintered at 1000 °C was exposed to heat treatment conditions in isothermal furnace for a holding time of 8 h. After 8-h period, the developed HEA was normalized in still air, and other samples were quenched in pure water. The third specimen was quenched at 4-h period and put back into the furnace and normalized after 8-h period, and it resulted in average microhardness of 847.46 HV. The microhardness result proves that heat treatment has a major influence on the thermal stability of the developed HEA. Drastic increase in microhardness values of 847.46 HV $Ti_{0.3}AlMoSi_{0.3}W_{0.1}$ was evident after 8 h of exposure to heat treatment conditions which was quenched at 4 h followed by normalizing after 8-h period in isothermal

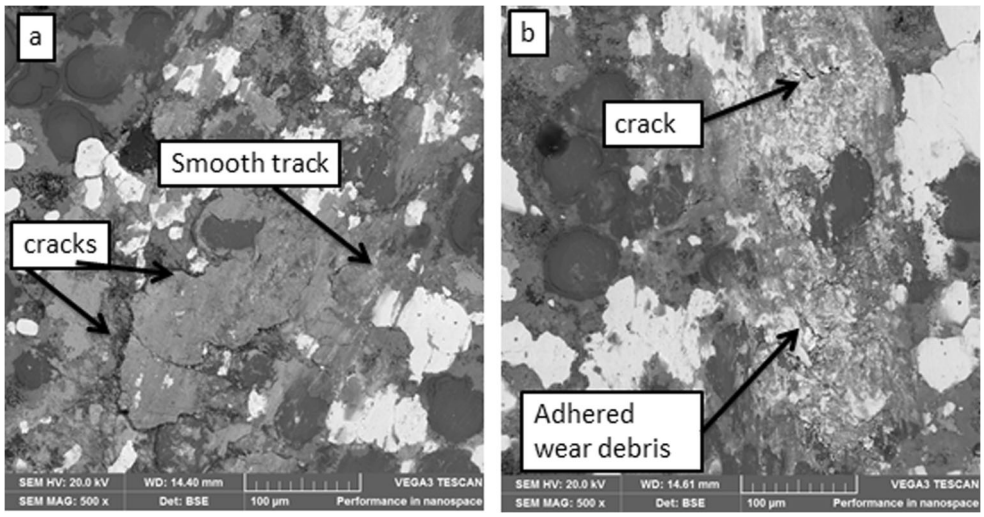

Fig. 10 Micrographs after wear tested of $Ti_{0.3}AlMoSi_{0.3}W_{0.1}$ HEA (**a**) 800 °C and (**b**) 1000 °C

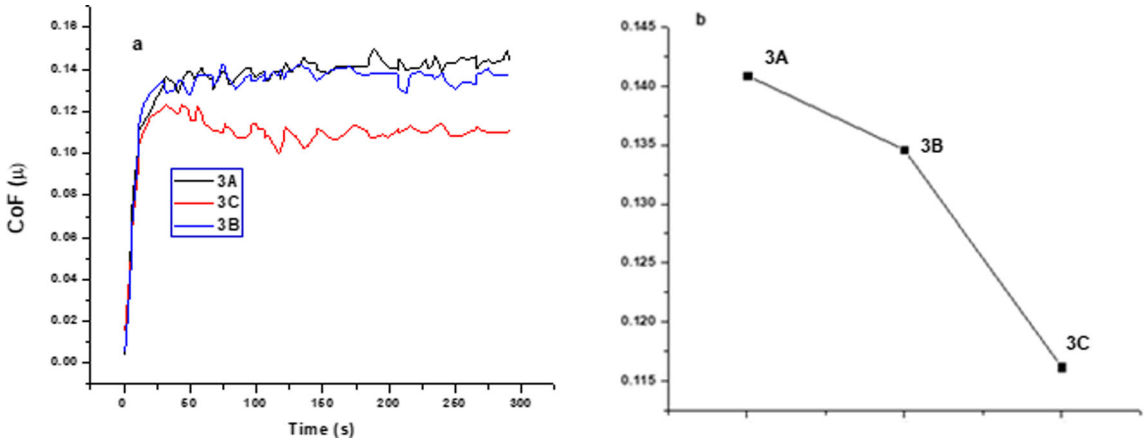

Fig. 11 CoF and average CoF for developed HEA sintered at various sintering temperature

furnace. 810.42 HV hardness value was observed in HEA which was directly quenched in water.

SEM images of heat-treated $Ti_{0.3}$-Al-Mo-$Si_{0.3}W_{0.1}$ high-entropy alloy sintered at 1000 °C are depicted in Fig. 14. The morphology displays different phases which consist of gray and light gray phases, white phase, and small black precipitated spot phases. The morphological evolution of the

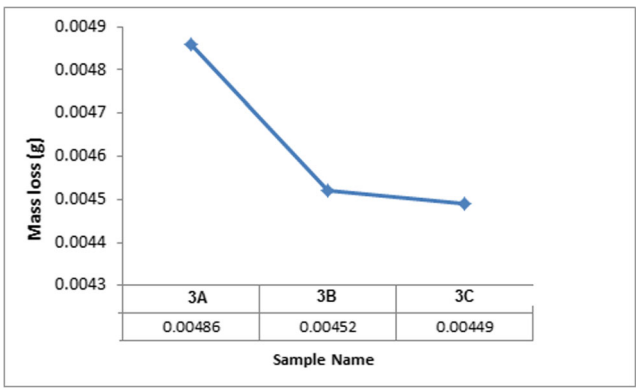

Fig. 12 Effect of sintering temperature on average wear mass loss

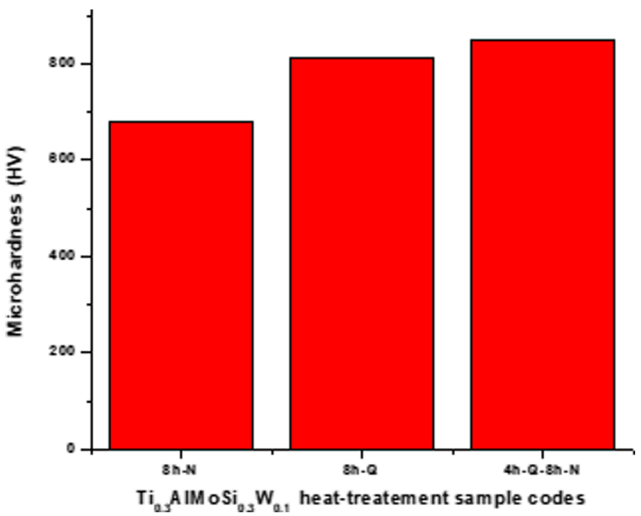

Fig. 13 Microhardness results of heat-treated $Ti_{0.3}AlMoSi_{0.3}W_{0.1}$ HEA

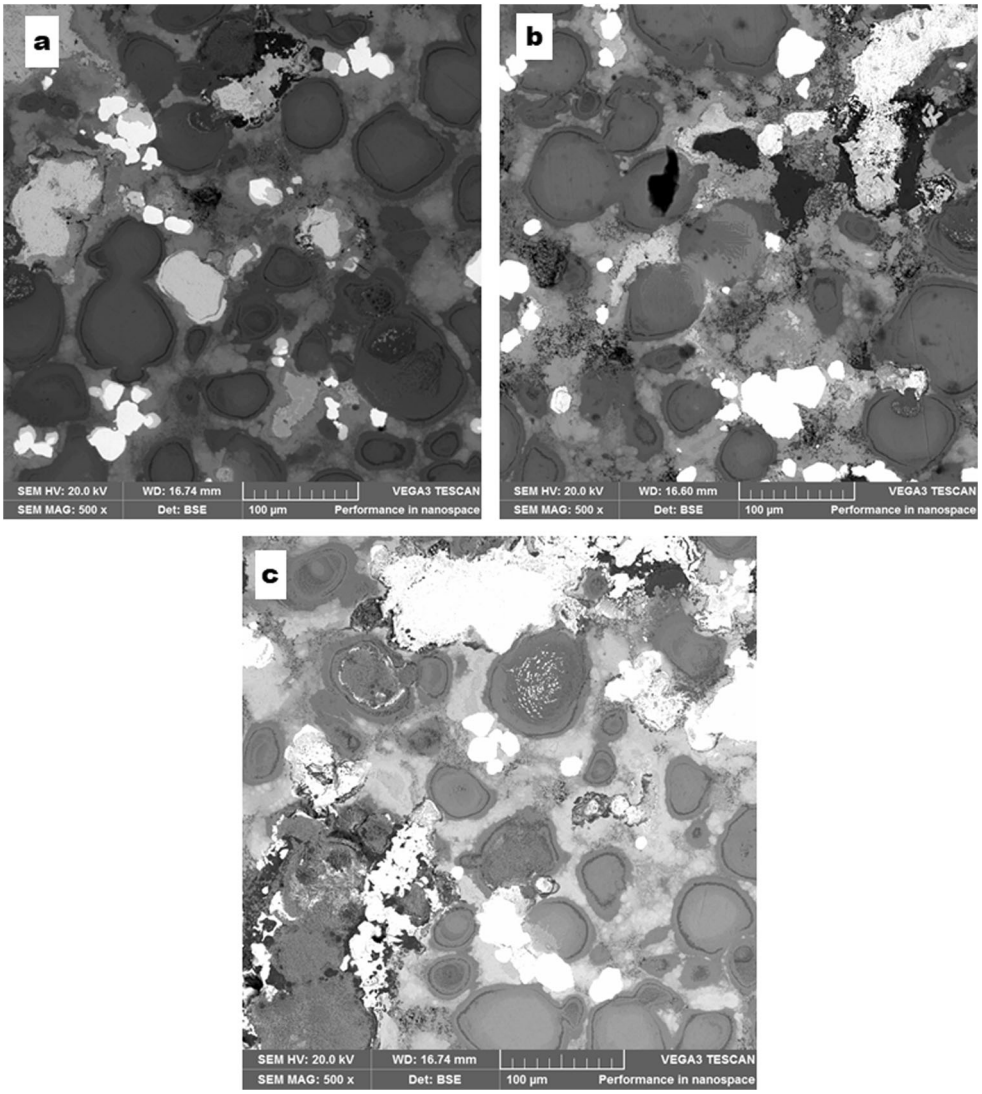

Fig. 14 SEM micrograph of heat-treated $Ti_{0.3}AlMoSi_{0.3}W_{0.1}$ sintered at 1000 °C HEA. (**a**) Normalized. (**b**) Quenched. (**c**) Quenched and normalized after 8 h

sample quenched (Fig. 14b) in pure water displays smaller grain size when compared to normalized HEA sample (Fig. 14a). This can be due to the fact that there is less phase transformation due to high cooling rate and fast nucleation which take place during quenching as compared to the normalized sample where the cooling medium is air. Normalizing heat treatment results in the sample holding heat for a longer period of time, and the cooling rate is slower, and therefore the growth of the grains is longer which results in coarse grain size. The microstructures of the heat-treated samples are also not homogeneous.

4 Conclusions

$Ti_{0.3}AlMoSi_{0.3}W_{0.1}$ HEA was consolidated using spark plasma sintering technology. The effect of sintering temperature on microstructural evolution, densification microhardness, wear, corrosion, oxidation, and thermal behavior of the developed HEA was studied.

- SEM image of the developed $Ti_{0.3}AlMoSi_{0.3}W_{0.1}$ HEA displays no cracks or initiation of stress. BCC phase along with intermetallic of $TiSi_2$, $MoSi_2$, and WSi_2 was identified on the microstructure.
- Maximum densification of 98.86% was achieved at sintering temperature of 1000 °C with microhardness of $764.63HV_{0.1}$, while sample sintered at 800 °C presented hardness of 521.44 HV with densification of 96.42%.
- Tribological study of the developed $Ti_{0.3}AlMoSi_{0.3}W_{0.1}$ HEA was found to be 0.1152 μ with a mass loss of 0.00449 g at consolidation temperature of 1000 °C.
- A maximum polarization resistance of 3712.02.Ω with corrosion rate of 0.004260 mm/year was achieved from the $Ti_{0.3}AlMoSi_{0.3}W_{0.1}$ alloy sintered at 1000 °C.

- $Ti_{0.3}AlMoSi_{0.3}W_{0.1}$ HEA sintered at 1000 °C showed less change in weight gain against temperature with minimum of 1.21 mg, while sample sintered at 900 °C showed mass gain of 1.29 mg.
- Thermal stability of the sintered HEA resulted in improved microhardness properties with maximum of 847.46 HV evident on the sample that went through quenching followed by normalizing at 8-h holding time.

Acknowledgments The authors would like to acknowledge the Institute for Nano Engineering Research, Surface Engineering Research Center, Tshwane University of Technology, Department of Chemical Metallurgical and Materials Engineering, Pretoria, South Africa, and also the Botswana International University of Science and Technology (BIUST).

References

1. Bhadeshia HKDH, Steve O (2012) Duplex hardening of steels for aeroengine bearings. ISIJ Int 52(11):1927–1934
2. Mouritz A (2012) Introduction to aerospace materials. Woodhead Publishing
3. Adesina O, Mthisi A (2017) The effect of laser based synthesized Ti-co coating on microstructure and mechanical properties of Ti6al4v alloy. Procedia Manufacturing 7:46–52
4. Farotade G, Popoola A, Pityana SL (2018) Influence of ZrB2 addition on microstructural development and microhardness of Ti-SiC clad coatings on Ti6Al4V substrate. Surf Rev Lett 25(06):1950005
5. Fatoba O, Adesina O (2018) Evaluation of microstructure, microhardness, and electrochemical properties of laser-deposited Ti-co coatings on Ti-6Al-4V alloy. Int J Adv Manuf Technol 97(5–8): 2341–2350
6. Kgoete F, Fayomi O, Adebiyi I (2018) Spark plasma sintered Ti-6Al-4V-Si3N4-TiN ternary composites: effect of combined microsized Si3N4 and TiN addition on microstructure and mechanical properties for aerospace application. J Alloys Compd 769:817–823
7. Makena MI et al (2017) Effect of sintering parameters on densification, corrosion and wear behaviour of Ni-50Fe alloy prepared by spark plasma sintering. J Alloys Compd 699:1166–1179
8. Olevsky EA, Froyen L (2009) Impact of thermal diffusion on densification during SPS. J Am Ceram Soc 92:S122–S132
9. Omori M (2000) Sintering, consolidation, reaction and crystal growth by the spark plasma system (SPS). Mater Sci Eng A 287(2):183–188
10. Shongwe MB et al (2018) Sintering behavior and effect of ternary additions on the microstructure and mechanical properties of Ni–Fe-based alloy. Part Sci Technol 36(5):643–654
11. Haase C, Barrales-Mora LA (2018) Influence of deformation and annealing twinning on the microstructure and texture evolution of face-centered cubic high-entropy alloys. Acta Mater 150:88–103
12. Kumar D et al (2018) Understanding the effect of tungsten on corrosion behavior of AlCuCrFeMnW x high-entropy alloys in 3.5 wt.% NaCl solution. J Mater Eng Perform 27(9):4481–4488
13. Li M et al (2018) Evaluation of microstructure and mechanical property variations in Al x CoCrFeNi high entropy alloys produced by a high-throughput laser deposition method. Intermetallics 95: 110–118
14. Waseem OA et al (2018) A combinatorial approach for the synthesis and analysis of Al x Cr y Mo z NbTiZr high-entropy alloys: oxidation behavior. J Mater Res 33(19):3226–3234
15. Cantor B et al (2004) Microstructural development in equiatomic multicomponent alloys. Mater Sci Eng A 375:213–218
16. Zhang Y et al (2008) Minor alloying behavior in bulk metallic glasses and high-entropy alloys. Sci China, Ser G 51(4):427–437
17. Mohanty S et al (2017) Powder metallurgical processing of equiatomic AlCoCrFeNi high entropy alloy: microstructure and mechanical properties. Mater Sci Eng A 679:299–313
18. Kang B et al (2018) Ultra-high strength WNbMoTaV high-entropy alloys with fine grain structure fabricated by powder metallurgical process. Mater Sci Eng A 712:616–624
19. Pohan RM et al (2017) Microstructures and mechanical properties of mechanically alloyed and spark plasma sintered Al0.3CoCrFeMnNi high entropy alloy. Mater Chem Phys:1–9
20. Wei J et al (2014) Mechanical alloying synthesis and spark plasma sintering consolidation of CoCrFeNiAl high-entropy alloy. J Alloys Compd 589:61–66
21. Zhang A et al (2016) Rapid preparation of AlCoCrFeNi high entropy alloy by spark plasma sintering from elemental powder mixture. Mater Lett 181:82–85
22. Yeh JW et al (2004) Nanostructured high-entropy alloys with multiple principal elements: novel alloy design concepts and outcomes. Adv Eng Mater 6(5):299–303
23. Zhang Y et al (2008) Solid-solution phase formation rules for multi-component alloys. Adv Eng Mater 10(6):534–538
24. Anselmi-Tamburini U et al (2004) Spark plasma sintering and characterization of bulk nanostructured fully stabilized zirconia: part I. Densification studies. J Mater Res 19(11):3255–3262
25. Gowon B et al (2015) The effects of sintering temperature on the densification of mechanically alloyed W-Brass composites. Open J Metal 5(03):19
26. Meir S et al (2009) Synthesis and densification of transparent magnesium aluminate spinel by SPS processing. J Am Ceram Soc 92(2):358–364
27. Lee C et al (2008) Effect of the aluminium content of AlxCrFe1. 5MnNi0. 5 high-entropy alloys on the corrosion behaviour in aqueous environments. Corros Sci 50(7):2053–2060
28. Sheng G, Liu CT (2011) Phase stability in high entropy alloys: formation of solid-solution phase or amorphous phase. Prog Nat Sci Mater Int 21(6):433–446
29. Yeh J-W et al (2004) Formation of simple crystal structures in cu-co-Ni-Cr-Al-Fe-Ti-V alloys with multiprincipal metallic elements. Metall Mater Trans A 35(8):2533–2536
30. Zhang Y et al (2014) Guidelines in predicting phase formation of high-entropy alloys. Mrs Communications 4(2):57–62
31. He J et al (2016) A precipitation-hardened high-entropy alloy with outstanding tensile properties. Acta Mater 102:187–196
32. Pickering E et al (2016) Precipitation in the equiatomic high-entropy alloy CrMnFeCoNi. Scr Mater 113:106–109
33. Huang C et al (2011) Thermal stability and oxidation resistance of laser clad TiVCrAlSi high entropy alloy coatings on Ti–6Al–4V alloy. Surf Coat Technol 206(6):1389–1395
34. Raphel A et al (2017) Oxidation and corrosion resistance of AlCoCrFeTiHigh entropy alloy. Mater Today Proc 4(2):195–202
35. Wu Q, Zhang JJ, Hao P, Ji Z, Dong S, Ling C, Chen Q, Wang J (2016) Versatile titanium silicide monolayers with prominent ferromagnetic, catalytic, and superconducting properties: theoretical prediction. J Phys Chem Lett 7(19):3723–3729
36. Sarkar AD (1980) Friction and wear. Academic Press, xvi+ 423, 23 x 15 cm, illustrated